IOP Publishing Plasma Physics and Controlled Fusion
Plasma Phys. Control. Fusion **62** (2020) 045018 (15pp) https://doi.org/10.1088/1361-6587/ab6a40

A limit-cycle model for internal transport barrier oscillations

A J Coelho[1], João P S Bizarro[1], B F A Silva[1] and X Litaudon[2,3]

[1] Instituto de Plasmas e Fusão Nuclear, Instituto Superior Técnico, Universidade de Lisboa, 1049-001 Lisboa, Portugal
[2] EUROfusion Programme Management Unit, Culham Science Centre, Culham, OX14 3DB, United Kingdom

E-mail: antonio.joao.coelho@tecnico.ulisboa.pt and bizarro@ipfn.tecnico.ulisboa.pt

Received 1 August 2019, revised 16 December 2019
Accepted for publication 10 January 2020
Published 26 February 2020

Abstract

A 0-D model for the time evolution of the electron temperature T and current density j is derived (following a systematic procedure) from the cylindrical 1-D electron heat transport and current density diffusion equations. The stationary regimes (stable fixed points) of the deduced dynamical system are analysed and it is shown that the model reproduces well the cases of total diffusion (no sources), of a pure Ohmic (OH) discharge and of a constant external heating scenario. Moreover, it is seen that, as the fraction of externally driven non-inductive current applied off-axis is increased, the system moves from an OH regime into an internal transport barrier (ITB) regime, where j is reversed and the negative magnetic shear reduces the heat diffusivity, thus increasing T at the core. When the external power deposition is made proportional to both T and j, limit-cycle oscillations, which resemble those of the O-regime at Tore Supra, are found. The 1-D transport equations are also solved numerically and an ITB oscillatory regime with features similar to the experiments is found, namely, a period of oscillation that is of the order of the resistive time scale, along with a decrease of the oscillation's amplitude with increasing frequency.

Keywords: internal transport barriers, limit-cycle oscillations, non-inductive current, advanced tokamak scenarios

(Some figures may appear in colour only in the online journal)

1. Introduction and motivation

The need to provide continuous electrical power to the grid from a fusion reactor is the basis of research on alternatives to the pulsed Ohmic (OH), inductive mode of tokamak operation [1–4]. This means that a steady state (SS) or a hybrid scenario, when plasma current is driven completely or partially by non-inductive (NI) methods, is one of the main goals in view of future reliable fusion reactors. Since, from an energetic point of view, it is economically prohibitive to rely solely on external NI current drive (CD) mechanisms, one must look for scenarios with a high fraction of bootstrap (BS) current [3, 5]. To achieve these scenarios, a highly tailored hollow current density profile is required [1, 4, 6], which can be created by means of some external NI CD applied off-axis. This induces a reversed profile for the safety factor q, i.e. an inner zone with negative magnetic shear, or a reversed shear (RS) region, that opposes the growth of drift wave instabilities, eventually stabilizing them [2]. Moreover, sheared $\mathbf{E} \times \mathbf{B}$ flows can reduce the amplitude of turbulent fluctuations. These two phenomena together result in a local decrease of the particle and heat turbulent diffusion coefficients, which can trigger the formation of an internal transport barrier (ITB), a region within the plasma core where the density and temperature gradients become large [2].

Whereas the radial heat flux $\mathbf{q}$ and density n are such that $\mathbf{q}/n \sim -\chi\nabla T$ stays essentially the same in this region of improved confinement, the temperature gradient ∇T in the plasma centre increases substantially (with a concomitant decrease of the diffusivity χ) [2], leading in this way to a

[3] Permanent address: CEA, IRFM, F-13108 Saint Paul Lez Durance, France.

higher value of the energy confinement time. This is the main reason why ITB's are a key factor in future operation of advanced tokamak (AT) scenarios. Notwithstanding this advantage, an oscillatory regime featuring long-lasting, quasi-sinusoidal electron temperature oscillations in the core has been measured in Tore Supra (and dubbed the O-regime) [7]. These oscillations are a result of a nonlinear coupling between electron temperature and current density and they are understood as the manifestation of an incomplete ITB transition, i.e. a regime that oscillates back and forth around a bifurcation to an enhanced core confinement state [8].

Similar oscillations have also appeared in fully NI experiments at TCV [9] and DIII-D [10] tokamaks, although in the latter case the oscillations are more of a relaxation type rather than sinusoidal. In Tore Supra, the onset of the oscillations is linked to a quasi-full lower-hybrid (LH) CD, which introduces a strong dependency of the current diffusion on the T and q profiles [11], but this coupling might also come from electron cyclotron (EC) heating and ECCD [9, 10], or even be found in high BS scenarios, since the BS current is also contingent on the T and q profiles. In all cases the oscillations have a very low frequency (1–10Hz) and are azimuthally and poloidally symmetric ($m = n = 0$), meaning that they are not of an MHD nature, although in Tore Supra [12] and TCV [9, 13] they have been seen to coexist with MHD modes, the latter eventually providing a good tool to diagnose these temperature oscillating regimes [12]. Nonetheless, an interplay between MHD modes and the q profile may indeed exist, so much so that no plasma discharge has been obtained in TCV displaying oscillations without the presence of MHD activity [13]. Differently from Tore Supra, in TCV the external NI current is driven by EC waves and the triggering of the oscillations has been concluded to be due to the destabilization of a large island caused by unfavourable q and pressure profiles [13].

Understanding the phenomenology underlying these oscillations, as well as the equations behind it, is of great importance, since this strong coupling between current and temperature may be a common feature of SS tokamak plasmas, and so we must know how to deal with it, especially when AT scenarios are one possibility for the operation of future tokamaks. So far, these oscillations have been analysed in the framework of the TASK/TR [14], ASTRA [15], CRONOS [8, 11] and JETTO [5, 16] transport codes, a link between Tore Supra's O-regime and a modified predator-prey dynamical system having also been presented [8]. The main motivation for this work is to tackle these oscillations also from a dynamical system point of view, but with a more consistent 0-D model derived systematically from the 1-D transport equations for heat and current density. This clearly differs from the previous predator-prey analysis [8], since the very simple noisy Lokta–Volterra equations used therein were introduced in an *ad hoc* fashion and not via an accurate reduction of the 1-D equations describing current diffusion and heat transport. Our approach is thus to look for limit-cycles (LC's), within our model, when these arise from an Andronov–Hopf (AH) bifurcation, a very common bifurcation in the study of dynamical systems, and one which is at the origin of an LC [17]. LC oscillations have already been invoked in the context of the L/H transition, namely to simulate the intermediary or dithering phases [18–21]. In one of these works, the same type of approach to be followed here was already used, i.e. to reduce a set of 1-D transport equations to a 0-D model by assuming certain spatial profiles and by subsequently evaluating the equations at a given position [18]. We also solve the more accurate 1-D equations and then compare the results with those of the 0-D model.

So, this paper is organized as follows: in section 2, the 0-D transport model (in the form of a dynamical system) is deduced from the 1-D equations and the heat diffusivities are adapted to the model; in section 3, the 0-D model is exploited, its SS cases are characterized and the conditions to see LC ITB oscillations are identified; in section 4 we discuss the numerical implementation of the 1-D equations and its results, and the latter are compared with those of the 0-D model; and, in section 5, we present a summary and the conclusions of our work.

2. Reduction of a 1-D to a 0-D model: from the transport equations to a dynamical system

2.1. Deriving the 0-D model

The transport equations for electron temperature T and current density j in cylindrical coordinates, assuming poloidal and axial symmetry, are given by [8, 14, 15]

$$\partial_t\left(\frac{3}{2}nT\right) = \frac{\partial_r(rn\chi\partial_r T)}{r} + S_\mathrm{h} \tag{1}$$

and

$$\mu_0\partial_t j = \frac{\partial_r[r\partial_r(\eta(j - j_\mathrm{NI}))]}{r}, \tag{2}$$

where n is the density, assumed to be constant, χ is the electron heat diffusivity and $\eta = \tilde{\eta}/T^{3/2}$ is Spitzer's resistivity with $\tilde{\eta} = 6.1 \times 10^{-8}\,\Omega\,\mathrm{m}$ if $[T] = \mathrm{keV}$ [6]. Note that, instead of using (2), it would also be possible to work with the diffusion equation for the poloidal magnetic field B_θ [14]

$$\partial_t B_\theta = \partial_r\left[\eta\left(\frac{1}{\mu_0}\frac{\partial_r(rB_\theta)}{r} - j_\mathrm{NI}\right)\right], \tag{3}$$

j and B being related by means of Ampère's law

$$j = \frac{1}{\mu_0}\frac{\partial_r(rB_\theta)}{r}. \tag{4}$$

The heating source term S_h in (1) comprises the sum of the OH heating plus external heating

$$S_\mathrm{h} = \eta j(j - j_\mathrm{NI}) + S_\mathrm{ext}, \tag{5}$$

the equipartition term being neglected[4]. The NI current j_NI in (2) is given as the sum of the BS current j_BS with some externally driven NI current j_ext. The expanded versions of (1)

[4] Basically, this approximation amounts to consider either that the ion and electron temperatures are roughly identical, and both equal to T, or that the latter is the sum of those two temperatures in a one-fluid model.

and (2) are thence

$$\frac{3}{2}n\partial_t T = n\left[\chi\frac{\partial_r T}{r} + (\partial_r\chi)(\partial_r T) + \chi\partial_r^2 T\right] + \eta j(j - j_{\mathrm{NI}}) + S_{\mathrm{ext}} \tag{6}$$

and

$$\mu_0\partial_t j = \left[\frac{\partial_r\eta}{r}j + \eta\frac{\partial_r j}{r} + (\partial_r^2\eta)j + 2(\partial_r\eta)(\partial_r j) + \eta\partial_r^2 j\right] - \left[\frac{\partial_r\eta}{r}j_{\mathrm{NI}} + \eta\frac{\partial_r j_{\mathrm{NI}}}{r} + (\partial_r^2\eta)j_{\mathrm{NI}} + 2(\partial_r\eta)(\partial_r j_{\mathrm{NI}}) + \eta\partial_r^2 j_{\mathrm{NI}}\right]. \tag{7}$$

The strategy now is to make a second-order expansion of $T(r, t)$ and $j(r, t)$ around the foot of the barrier r_{b}, which we are going to fix; the temperature and current density values at this position, T_{b} and j_{b}, respectively, are also to be fixed. Furthermore, we require the boundary conditions on the axis as follows: $j'(r = 0) = T'(r = 0) = 0$. Thus, choosing profiles compatible with these conditions, we set

$$T(r) = T_0 - (T_0 - T_{\mathrm{b}})\left(\frac{r}{r_{\mathrm{b}}}\right)^2 \tag{8}$$

and

$$j(r) = j_0 - (j_0 - j_{\mathrm{b}})\left(\frac{r}{r_{\mathrm{b}}}\right)^2, \tag{9}$$

the time dependency entering via the on-axis quantities $T_0 \equiv T_0(t)$ and $j_0 \equiv j_0(t)$. The NI current term is treated also with a second order expansion, being given by $j_{\mathrm{NI}} = j_{\mathrm{NI_b}}(r/r_{\mathrm{b}})^2$ with $j_{\mathrm{NI_b}} = j_{\mathrm{BS_b}} + j_{\mathrm{ext_b}}$. So, after inserting these profiles in (6) and (7), and evaluating both equations at $r = 0$, the two coupled partial differential equations (PDE's) become a nonlinear autonomous dynamical system of two ordinary differential equations (ODE's), namely,

$$\frac{3}{2}n\left(\frac{\partial_t T_0}{T_{\mathrm{b}}}\right) = -\frac{4n\chi}{r_b^2}\left(\frac{T_0}{T_{\mathrm{b}}} - 1\right) + \frac{\eta_{\mathrm{b}} j_{\mathrm{b}}^2}{T_{\mathrm{b}}}\left(\frac{T_{\mathrm{b}}}{T_0}\right)^{3/2}\left(\frac{j_0}{j_{\mathrm{b}}}\right)^2 + \frac{S_{\mathrm{ext}}(r = 0)}{T_{\mathrm{b}}} \tag{10}$$

and

$$\mu_0\left(\frac{\partial_t j_0}{j_{\mathrm{b}}}\right) = 2\left[\frac{3\eta_{\mathrm{b}}}{r_{\mathrm{b}}^2}\left(\frac{T_0}{T_{\mathrm{b}}} - 1\right)\left(\frac{T_{\mathrm{b}}}{T_0}\right)^{5/2}\frac{j_0}{j_{\mathrm{b}}} - \frac{2\eta_{\mathrm{b}}}{r_{\mathrm{b}}^2}\left(\frac{T_{\mathrm{b}}}{T_0}\right)^{3/2}\left(\frac{j_0}{j_{\mathrm{b}}} - 1\right)\right] - 4\frac{\eta_{\mathrm{b}}}{r_{\mathrm{b}}^2}\left(\frac{T_{\mathrm{b}}}{T_0}\right)^{3/2}\left(\frac{j_{\mathrm{BS}_b}}{j_{\mathrm{b}}} + \frac{j_{\mathrm{ext}_b}}{j_{\mathrm{b}}}\right). \tag{11}$$

The time-varying value of the BS current at the barrier's foot $j_{\mathrm{BS_b}}$ is evaluated from the known BS expression [22]

$$j_{\mathrm{BS}}(r) = -4.3 \times 10^3\left(\frac{r}{R_0}\right)^{1/2}\frac{n_{20}}{B_\theta(r)}\partial_r T, \tag{12}$$

where R_0 is the major radius of the tokamak and all quantities are in SI units except T and n_{20}, which are to be given in keV and $10^{20}\,\mathrm{m}^{-3}$, respectively. Using the expanded profiles (8) and (9) we get, after some simple algebra,

$$j_{\mathrm{BS_b}} = 3.5 \times 10^4\frac{n_{20}}{\mu_0 R_0^{1/2} r_{\mathrm{b}}^{3/2}}\frac{T_0 - T_{\mathrm{b}}}{j_0 + j_{\mathrm{b}}}. \tag{13}$$

Note that this is in accordance with what one would expect from a BS current: increases with increasing T_0 for a fixed value of T_{b} (i.e. the gradient at the barrier's foot is higher) and becomes zero if the gradient is zero (i.e. if $T_0 = T_{\mathrm{b}}$). We fix the external NI current to a constant value according to $j_{\mathrm{ext_b}}/j_{\mathrm{b}} \equiv K_{\mathrm{NI}}$, and we further define the adimensional quantities $x \equiv T_0/T_{\mathrm{b}}$ and $y \equiv j_0/j_{\mathrm{b}}$, which are to be of great use in what follows.

2.2. Choosing heat diffusivities for the 0-D model

The only quantity in (10) and (11) we have not yet provided is the electron heat diffusivity χ. Currently, a first-principles derived heat diffusivity taking into account the negative magnetic shear effect is still lacking. Indeed, transport simulations typically use an heuristic model that mimics the reduction of the coefficients in the presence of an RS configuration [11, 24, 23]. In the present work we use two different forms for the diffusivity, the first and simplest one being a phenomenological model that captures the essence of the influence the magnetic shear s has in reducing χ: for $s < 0$, the heat diffusivity tends to a lower value (i.e. χ_{H} for high-confinement mode) whereas, for $s > 0$, approaches a higher value (i.e. χ_{L} for low-confinement mode). By casting this behaviour in a logistic function as is done in common transport codes [11, 15], the henceforth called shear diffusivity reads

$$\chi_{\mathrm{sh}} = \chi_{\mathrm{H}} + \frac{\chi_{\mathrm{L}} - \chi_{\mathrm{H}}}{1 + e^{-\alpha s}}, \tag{14}$$

with α a shear control parameter. In cylindrical coordinates, the magnetic shear is given by [6, 22]

$$s \equiv \frac{r}{q}\frac{\mathrm{d}q}{\mathrm{d}r} = 2 - \frac{r^2 j(r)}{\int_0^r r' j(r') dr'} = 1 - \frac{r\partial_r B_\theta(r)}{B_\theta(r)}. \tag{15}$$

This is a complicated function of j, hence the importance to realize that, within our model, $y > 1$ corresponds to a typical

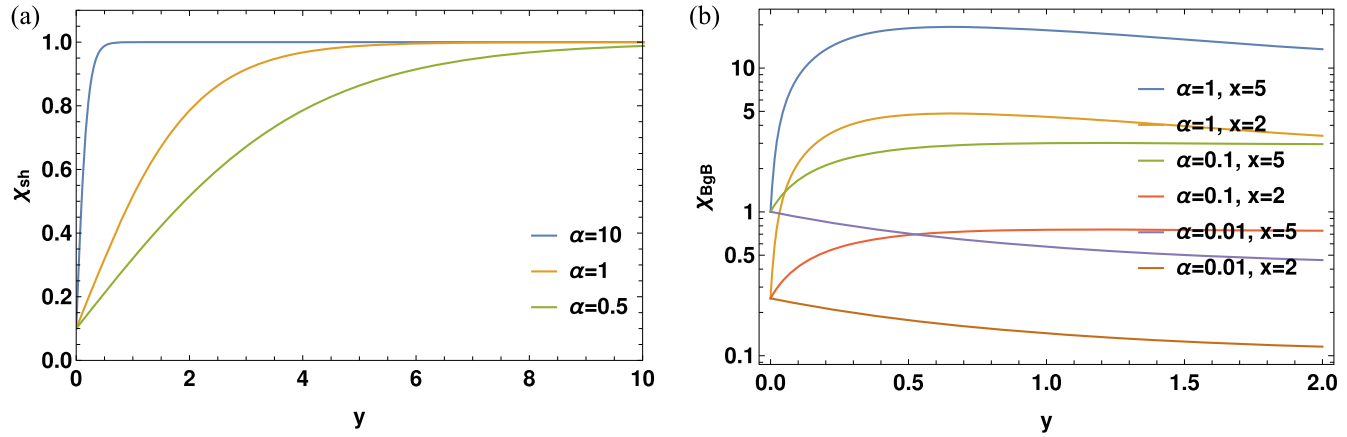

Figure 1. (a) Shear diffusivity $\chi = \chi_{sh}(y)$, as given by (16), and (b) BgB diffusivity $\chi = \chi_{BgB}(x, y)$, as given by (23) with $\gamma = 0.01$. Note that in both cases α controls the slope of the curves and that these models are only valid for $y \geqslant 0$.

OH non-reversed discharge, whereas $y < 1$ corresponds to an RS configuration. Thus we have the correspondence $\chi \to \chi_H$ as $y \to 0$ and $\chi \to \chi_L$ as $y \to +\infty$:

$$\chi_{sh} = 2\chi_H - \chi_L + 2\frac{\chi_L - \chi_H}{1 + e^{-\alpha y}}, \tag{16}$$

a graphical representation being shown in figure 1(a). We now fix $\chi_H = 0.1\,\mathrm{m^2\,s^{-1}}$ and $\chi_L = 1.0\,\mathrm{m^2\,s^{-1}}$, because turbulent diffusion coefficients in fusion plasmas are typically of the order of $1.0\,\mathrm{m^2\,s^{-1}}$ [6], and we further assume that negative magnetic shear can potentially reduce them up to one order of magnitude, as inferred from the O-regime simulations for Tore Supra using the CRONOS transport code [8].

The second form for the diffusivity used in this work is more sophisticated and takes into account temperature, as is usual for a diffusion coefficient in a fusion plasma. Without an RS configuration, turbulent diffusion coefficients usually follow the Bohm (B) and gyro-Bohm (gB) forms, respectively,

$$\chi_B = C_1 \frac{a}{B_0} q^2 \left| \frac{dT}{dr} \right| \tag{17}$$

and

$$\chi_{gB} = C_2 \frac{\sqrt{T}}{B_0^2} \left| \frac{dT}{dr} \right|, \tag{18}$$

with $C_{1,2}$ numerical coefficients usually adjusted by benchmarking to a broad range of discharges and the total diffusion coefficient being given by $\chi = \chi_B + \chi_{gB}$ [24, 25]. Whenever the shear effect is to be taken into account, a shear function $F(s)$ multiplies the B term (i.e. $\chi = F(s)\chi_B + \chi_{gB}$), so that its value becomes reduced in an RS configuration [11, 23]. The B term is related with the long-wavelength turbulence transport and it is this one that is reduced in the region with low-positive or negative magnetic shear, the short-wavelength turbulence, which produces gB transport, being not modified in such a region [24]. Using profiles (8) and (9), and evaluating the diffusivity inside the barrier at $r = r_b$[5], we get

$$\chi_B = \underbrace{C_1 \frac{2aB_0}{r_b}\left(\frac{4}{R_0\mu_0 j_b}\right)^2 T_b}_{C_1'} \frac{|x-1|}{(y+1)^2} \tag{19}$$

and

$$\chi_{gB} = \underbrace{C_2 \frac{2\sqrt{T_b}}{B_0^2 r_b} T_b}_{C_2'} |x-1|. \tag{20}$$

Plugging in (19) and (20) the Tore Supra values $R_0 = 2.4\,\mathrm{m}$, $a = 0.7\,\mathrm{m}$, $r_b = 0.2a$, $B_0 = 3.8\,\mathrm{T}$, $n_{20} = 0.5\,\mathrm{m^{-3}}$, $T_b = 4\,\mathrm{keV}$, $\eta_b = 8 \times 10^{-9}\,\Omega\,\mathrm{m}$, $j_b = 1.5\,\mathrm{MA\,m^{-2}}$ [8], we obtain $C_1' = 119$ and $C_2' = 7.91$. When all constants are given in SI units, except for T_b, which is given in keV, $C_1 = 0.200$ and $C_2 = 0.158$ for electrons [25]. This means that $C_1C_1' = 23.8\,\mathrm{m^2\,s^{-1}}$ and $C_2C_2' = 1.26\,\mathrm{m^2\,s^{-1}}$, so we can put

$$\chi_B = C_1C_1' \frac{|x-1|}{(y+1)^2} \tag{21}$$

and

$$\chi_{gB} = C_2C_2'|x-1|. \tag{22}$$

Introducing now a shear function that multiplies both B and gB terms, in order to amplify the shear effect [11], we write the BgB diffusivity as

$$\chi_{BgB} = (\chi_B + \chi_{gB})[1 - (1-\gamma)e^{-\alpha y}], \tag{23}$$

with the γ factor preventing $\chi_{BgB} \to 0$ when $y \to 0$. Thus, if for instance $\gamma = 0.01$, the total diffusivity is reduced by two orders of magnitude as $y \to 0$. In figure 1(b) we plot the trend of χ_{BgB} with y for some values of x and α. It can be seen that, just like with χ_{sh}, for small y and α above a certain threshold, we have that the diffusivity decreases as the

[5] The reason why we do not evaluate it at the core (i.e. at $r = 0$) is because (17) and (18) vanish there, meaning that we would lost the heat diffusion term from our model.

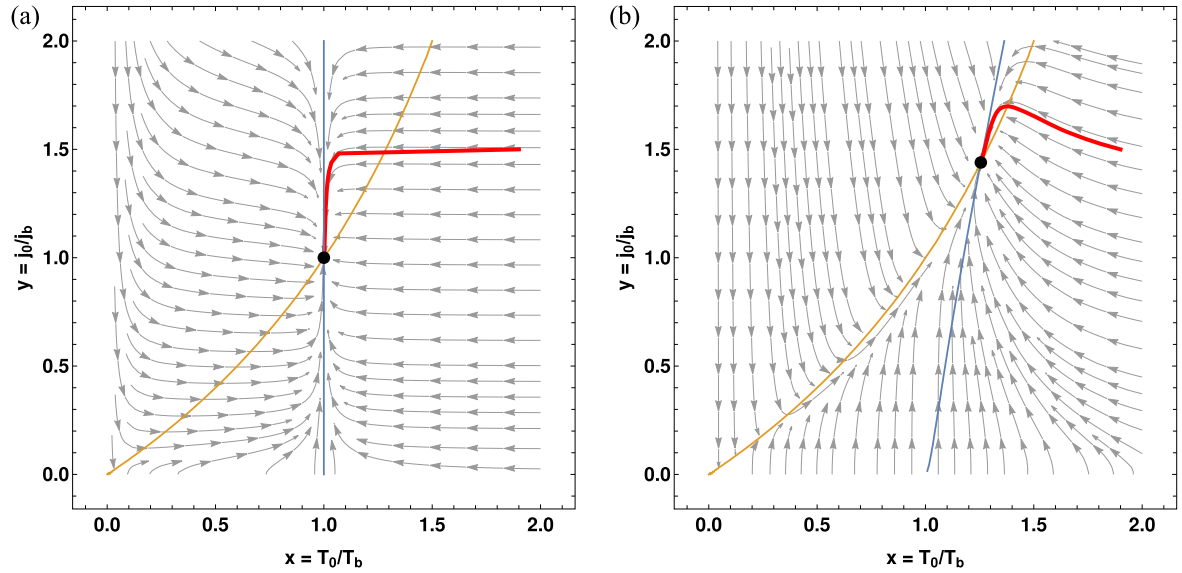

Figure 2. Phase space and vector field of (24) and (25) for (a) $C_\Omega = 0$ and $\mu = 0.001$ and (b) $C_\Omega = 0.02$ and $\mu = 0.1$, with $\chi = \chi_{\mathrm{BgB}}$ ($\alpha = 1.0$) and $C_{\mathrm{BS}} = K_{\mathrm{ext}} = K_{\mathrm{NI}} = 0$. Blue and orange lines are the x- and y-nullclines, respectively, the red curves correspond to some trajectories in phase space and the black dots indicate the stable fixed points $\{x_{\mathrm{SS}}, y_{\mathrm{SS}}\}$.

profile becomes more reversed (i.e. y becomes smaller than 1); then, as y becomes large, χ_{BgB} tends approximately to a constant value. For a sufficiently small value of α, however, the denominator of the B term starts to take a role and χ_{BgB} decreases with y. Nonetheless, for both small and large α, the dependence on the temperature gradient is very clear: χ_{BgB} increases with x.

2.3. Nondimensionalising the 0-D model

By defining $\tau_x \equiv r_{\mathrm{b}}^2/\chi_0$, $\tau_y \equiv \mu_0 r_{\mathrm{b}}^2/\eta_{\mathrm{b}}$, $C_\Omega \equiv 4.20 \times 10^{-5} r_{\mathrm{b}}^2 \eta_{\mathrm{b}} j_{\mathrm{b}}^2 / n_{20} T_{\mathrm{b}} \chi_0$, $C_{\mathrm{BS}} \equiv 3.5 \times 10^4 n_{20} T_{\mathrm{b}} / \mu_0 R_0^{1/2} r_{\mathrm{b}}^{3/2} j_{\mathrm{b}}^2$ and $(2r_{\mathrm{b}}^2/3nT_{\mathrm{b}}\chi_0) S_{\mathrm{ext}}(r=0) \equiv K_{\mathrm{ext}} h(x, y)$, (10) and (11) can be rewritten in an adimensional form as

$$\tau_x \dot{x} = -\frac{8}{3}\widetilde{\chi}(x, y)(x - 1) + C_\Omega \frac{y^2}{x^{3/2}} + K_{\mathrm{ext}} h(x, y) \quad (24)$$

and

$$\tau_y \dot{y} = \frac{4}{x^{3/2}}\left[\frac{3}{2}\frac{y}{x}(x - 1) - (y - 1) - C_{\mathrm{BS}}\frac{x - 1}{y + 1} - K_{\mathrm{NI}}\right]. \quad (25)$$

Hereabove $\widetilde{\chi} \equiv \chi/\chi_0$, with χ given by (16) or (23) and χ_0 a normalization constant equal to χ_{L} or $C_{\mathrm{l}} C_{\mathrm{l}}'$, respectively. Using Tore Supra values, we have $C_{\mathrm{BS}} = 0.305$, $\tau_y = 3.08$ s, $\tau_x = 1.96 \times 10^{-2}$ or 8.24×10^{-4} s, and $C_\Omega = 7.41 \times 10^{-3}$ or 3.11×10^{-4}, depending on the form chosen for χ (i.e. whether χ_{sh} or χ_{BgB}).

It is tempting to regard τ_x and τ_y as the heat transport and current diffusion time scales, respectively. If this poses no problem with the latter, regarding the former there is a very strong dependency on the model chosen for χ, which may lead to very disparate figures for τ_x, as we have just seen. As such, we no longer look at τ_x as being fixed by the χ model, but we consider it an independent parameter instead, to be gauged against τ_y through the ratio $\mu \equiv \tau_x/\tau_y$[6]. One of the unresolved issues of AT studies is precisely the scaling of the energy confinement time, and thus also of χ, with plasma parameters [15]. Typically, it is difficult to find such scaling because of the strong coupling between the plasma quantities, in this case between j and T. This uncertainty that still exists regarding the χ models for AT scenarios gives us some liberty to take τ_x as a free parameter. Note as well that α, K_{NI} and K_{ext} are free parameters of the model and $h(x, y)$ is a function that may, or may not, depend on x and y, depending on which external heating scheme is under consideration.

3. Discussion of the 0-D model: results from a dynamical system

3.1. Testing the simplest cases

The best way to test our model is to make sure that the outcome is correct when looking at familiar situations. We thus start to study the dynamical system in its simplest form (i.e. with no sources) and then successively add more terms.

3.1.1. No sources. Let us then start by setting all heating and current sources to zero in (24) and (25), that is, by making $C_\Omega = K_{\mathrm{ext}} = C_{\mathrm{BS}} = K_{\mathrm{NI}} = 0$. In this case, the system has the fixed point $\{x_{\mathrm{SS}} = 1,\ y_{\mathrm{SS}} = 1\}$, which is a stable node regardless of the form of the diffusivity used. Furthermore,

[6] In fact, (24) and (25) can be written without explicit dependence on τ_x and τ_y individually, but rather with a single dependence on μ if time t is normalized to one of those characteristic time scales.

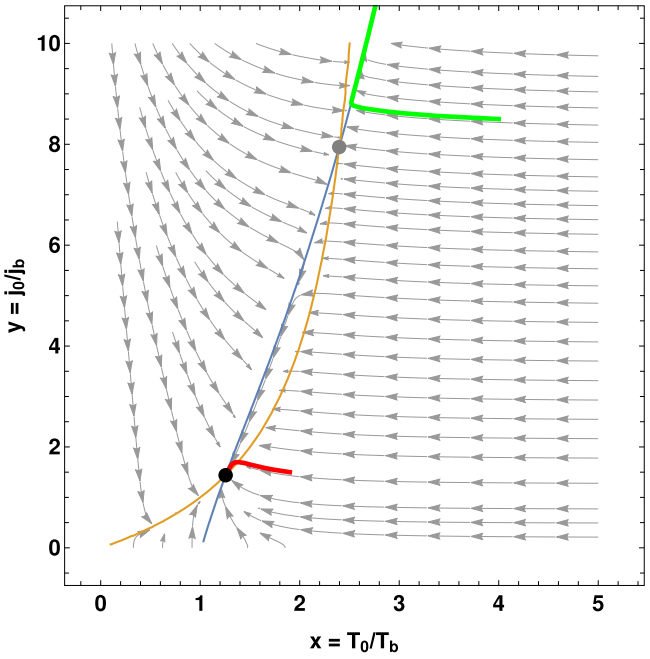

Figure 3. Zoomed-out view of figure 2(b), where it is possible to see an unstable fixed point (grey dot) and a new trajectory (green line) starting at a large y value and thus failing to be attracted to the stable fixed point (black dot), but rather diverging to infinity.

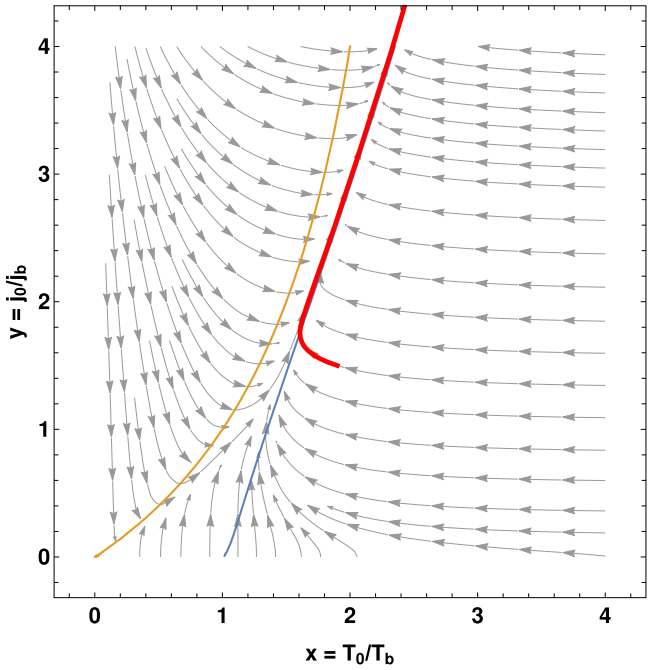

Figure 4. Phase space and vector field of (24) and (25) for $C_\Omega = 0.1 > C_\Omega^{MAX}$ and $\mu = 0.1$, with $\chi = \chi_{BgB}$ ($\alpha = 1.0$) and $C_{BS} = K_{ext} = K_{NI} = 0$. Blue and orange lines are the x- and y-nullclines, respectively, and the red curve corresponds to some trajectory in phase space.

whatever the initial conditions are, the system evolves always towards its stable node. This result is indeed consistent with our knowledge of transport equations: with no sources, the temperature and the current simply diffuse away, achieving an SS where T and j are everywhere equal to their boundary values. Recalling that T and j are actually normalized to the boundary values T_b and j_b, this SS corresponds to having $x = 1$ and $y = 1$, as can be seen in figure 2(a). Note that the trajectory is rapidly attracted to the x-nullcline[7], and then slowly approaches the stable equilibrium, which is due to the distinct time scales we have set for this simulation. In addition, keep in mind that any SS equilibrium $\{x_{SS}, y_{SS}\}$ is independent of the time scales.

3.1.2. OH heating. If $C_\Omega \neq 0$, the stable node verifies $\{x_{SS} > 1, y_{SS} > 1\}$, as shown in figure 2(b), which is also expected because, in principle, it is possible to sustain non-constant temperature and current density profiles whenever there is a source term balancing the diffusion losses. However, note that for the realistic value of C_Ω used in the simulation, x_{SS} is very close to 1, meaning that it is not possible to sustain large temperature gradients inside the ITB solely with OH heating. Note as well that, if the initial y value $y(0)$ is too large, the system diverges (i.e. $x \to \infty$ and $y \to \infty$). This is simply due to the fact that the OH heating scales with y^2 and so, if the initial y is too large, the heating quickly overcomes the diffusion losses (in the case that $\dot{x}(0) < 0$, otherwise the losses are initially already overcome), driving the system to higher and higher temperatures. On the other hand, the reason for y not stabilizing can be explained by rewriting (25) in the case with no current sources as

$$\dot{y} = \frac{4}{x^{3/2}}\left[\frac{y}{2}\left(1 - \frac{3}{x}\right) + 1\right], \tag{26}$$

which shows that y does not stabilize if $x > 3$. This can be verified in figure 3, a zoomed-out view of figure 2(b), where it is possible to see an unstable fixed point at very large y, with the green trajectory, which starts with a very large $y(0)$, failing to be attracted to the stable fixed point but rather diverging to infinity. Note however that this indefinitely growth of y is non-physical since, in an OH discharge, the total plasma current is fixed and, thus, the central current density could only go ideally to infinity if j were zero everywhere else. The actual term that makes this behaviour possible is the one that comes from the first and second derivatives of the resistivity, and the fact that our model allows this behaviour is probably due to some simplifying assumption made. Incidentally, note that $x \to \infty$ is also non-physical because the pressure, hence the temperature, is limited by the β-limit in a tokamak plasma [6, 22]. Indeed, this is one of the main operational issues related with ITB's: if the barrier becomes too good, the pressure overcomes its limit value and a disruption occurs due to MHD instability [2–4]. Remark still that in figure 2(b) we have used a much larger value for μ than that of figure 2(a), and because of this we can see that the trajectory is no longer rapidly attracted to the x-nullcline.

Another feature of the model is that C_Ω cannot be too large, otherwise the stable node is lost (i.e. the nullclines no longer cross each other to produce a stable fixed point) and the system diverges whatever the initial condition, as shown

[7] The x- and y-nullclines are the set of points where $\dot{x}$ and $\dot{y}$ are zero, respectively.

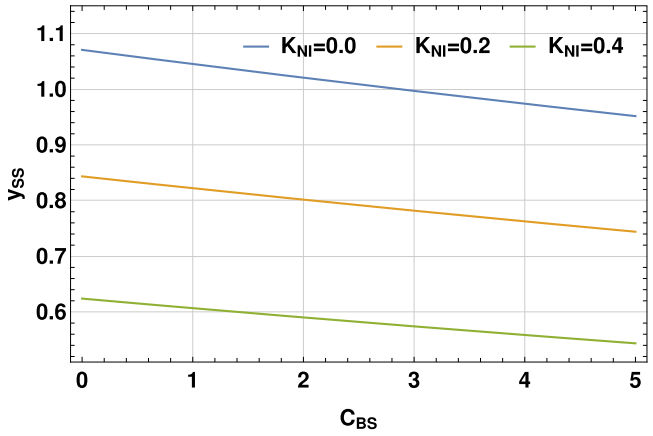

Figure 5. Stable fixed point y_{SS} as a function of C_{BS} for different K_{NI} and with $C_\Omega = 0.001$, $\chi = \chi_{BgB}$ ($\alpha = 1.0$) and $K_{ext} = 0$.

in figure 4. Once more, this is due to the large heating when compared with the losses: if C_Ω is too large, then the OH heating eventually drives the system to a point where $x > 3$, thus pushing the y-equation into an unstable region and consequently, with OH heating increasing simultaneously with y, driving x even further up. Nevertheless, it should be mentioned that the value C_Ω^{MAX} above which the stable node is lost is orders of magnitude above the C_Ω values previously calculated using Tore Supra parameters.

3.1.3. BS and NI currents. Let us now release the constraint $C_{BS} = 0$ and recall that in highly bootstrapped tokamak plasmas, when the BS current gets peaked off-axis, the total current density follows and, eventually, gets peaked at the same position [4, 5, 10]. In our 0-D model this signifies that, if we have an initial situation with $y > 1$ and at some point j_{BS_b} starts to increase, the total current density starts changing to a more RS profile, meaning that y begins decreasing, eventually reaching $y < 1$ if the BS term at the barrier grows even further. With this in view, observe from (25) that a growth in the BS term always contributes to reduce $\dot{y}(t)$; moreover, we find from figure 5 that the y_{SS} value decreases with increasing C_{BS}. These two features of our model are thus in good agreement with the physics we just discussed and that usually happens in tokamak plasmas. In addition, note that when we make $K_{NI} \neq 0$ we have the same effect as when $C_{BS} \neq 0$, implying that, if both C_{BS} and K_{NI} do not vanish, more easily y_{SS} reaches a lower value.

3.1.4. External heating. If we now set $h(x, y) = 1$ and K_{ext} a positive constant, we can find the behaviour of the system when it is externally heated at the core. It is thus found that there is a stable node for $0 < K_{ext} < K_{ext}^{MAX}$, and beyond K_{ext}^{MAX} the nullclines no longer cross and the system diverges independently of the initial condition. In the region where the system converges to a stable node, the value of x_{SS} increases with K_{ext}, which means that more external heating leads to a higher core SS temperature. The value of y_{SS} also grows with K_{ext} because, with higher temperatures, the resistivity is smaller and so the current can penetrate further into the core. In fact, y_{SS} increases much faster than x_{SS} with K_{ext} as can be seen in figure 6, where it is depicted the evolution of x_{SS} and y_{SS} with K_{ext} for three different values of C_Ω. It is possible to see that, with increasing C_Ω, K_{ext}^{MAX} decreases; in other words, if the OH heating increases, there is, say, less room for the system to be externally heated without diverging. Moreover, the highest x_{SS} value increases with decreasing C_Ω, with the highest value of $x_{SS} \to 3$ and $y_{SS} \to \infty$ in the limit $C_\Omega \to 0$, which is consistent with what we have seen in connection with the analysis of OH heating.

3.2. Analysing ITB regimes

In the $h(x, y) = 1$, $K_{ext} > 0$ and $K_{NI} > 0$ case, it should be possible to observe two different SS regimes: an OH and an ITB, depending on the external parameters K_{ext} and K_{NI}, and independently of the diffusivity used, whether χ_{sh} or χ_{BgB}. Whereas in an OH SS situation we expect $x_{SS} \gtrsim 1$ and $y_{SS} \gtrsim 1$, in the case of an ITB SS with RS we ought to find $x_{SS} \gg 1$ and $y_{SS} \lesssim 1$.

3.2.1. SS ITB's. The phase spaces corresponding to SS OH and ITB regimes are shown in figures 7(a) and (b), respectively, where K_{ext} is fixed but the fraction K_{NI} of externally applied NI current is different. Then, in figures 8(a) and (b) we plot x_{SS} and y_{SS} as a function of K_{NI} and for different K_{ext}. The first thing to notice is that, in general, x_{SS} increases with K_{NI}, which means that, as the fraction of external NI current applied at the foot of the barrier increases, so does the temperature; this is just a consequence of y_{SS} being decreasing, reducing in this way the diffusivity (16). Hence, we can conclude that, as K_{NI} is increased, the system moves from an SS OH regime into an SS ITB regime, in which the externally applied NI current changes the current density into a reversed profile, reducing the turbulent transport and thus allowing for steeper temperature gradients at the core.

One note regarding the small decreasing of x_{SS} with K_{NI} at small values of the latter for $K_{ext} = 4.0$ in figure 8(a). This is due to the fact that, for large K_{ext} and small K_{NI} (and thus very large y_{SS}), the heating sources (i.e. OH and external) overcome the diffusion term. Indeed, when $K_{NI} < 0.1$ there is no solution (i.e. the nullclines do not cross to produce a stable fixed point) because the heating becomes so large that it is not compensated by diffusion, driving the system to an unstable situation where temperature keeps increasing indefinitely. If C_Ω is set to zero, this behaviour is no longer seen. Remark, in addition, that y_{SS} also increases with K_{ext}, which is due to the first term on the right-hand side of (25), the one that arises from the radial derivatives of η.

Still referring to figures 7(a) and (b), note that in both we have plotted two trajectories starting at different initial conditions. In the case of the SS ITB regime in figure 7(b), where K_{NI} has a larger value than in the SS OH case, for a too small $y(0)$ the system is not attracted to the stable fixed point, but rather diverges away with temperature continuously increasing as seen in the green trajectory. Indeed, we have found that for any $0 < K_{ext} < K_{ext}^{MAX}$, as K_{NI} increases, $y(0)$ at

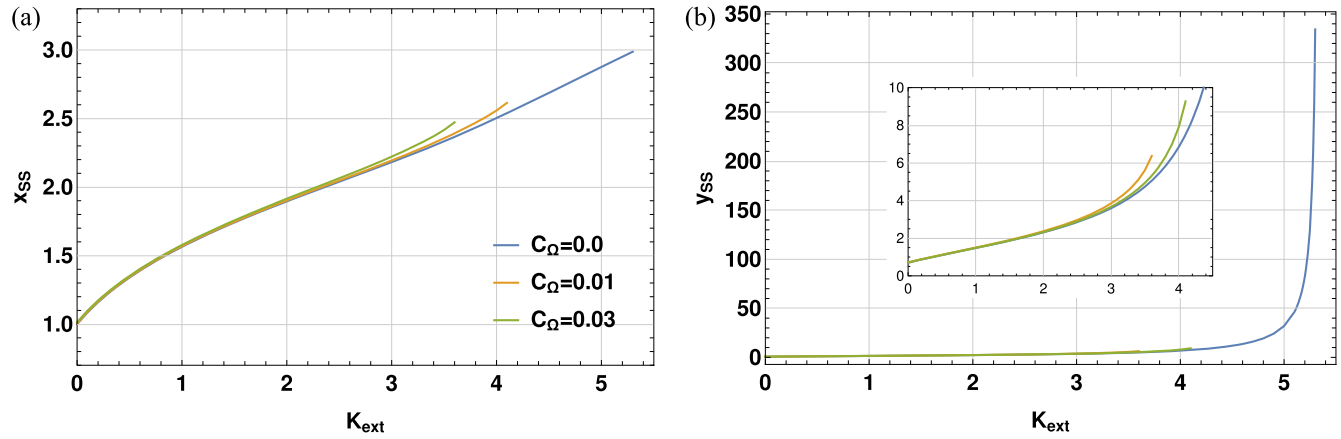

Figure 6. Stable fixed points x_{SS} and y_{SS}, respectively (a) and (b), as functions of K_{ext} for different C_Ω and with $\chi = \chi_{sh}$ ($\alpha = 1.0$), $C_{BS} = 0.1$, $K_{NI} = 0.3$ and $h(x, y) = 1$.

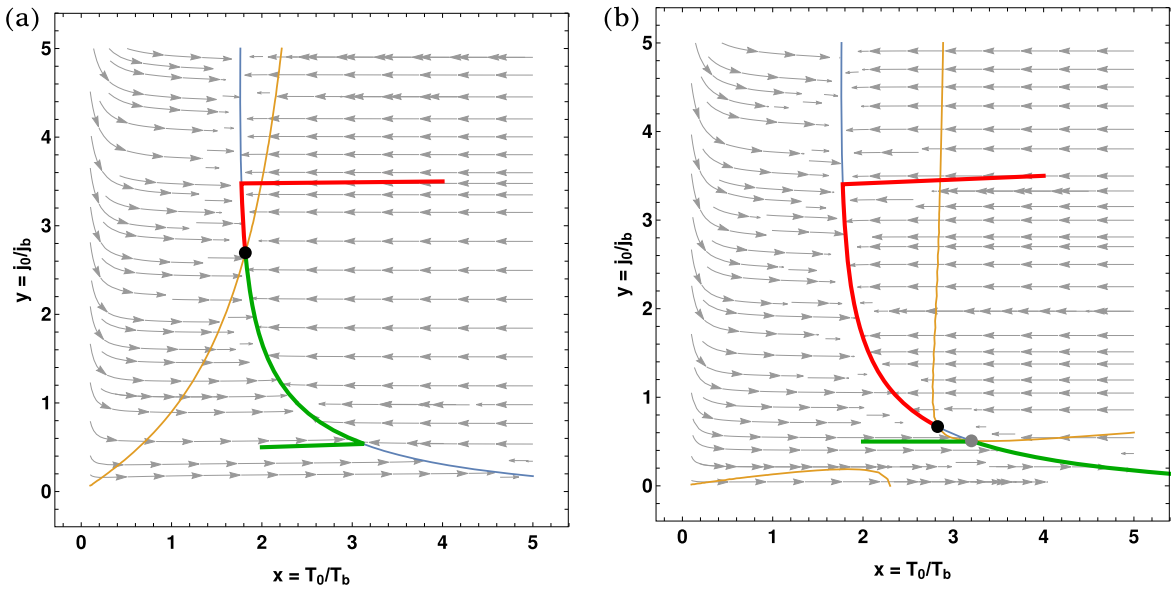

Figure 7. Phase space and vector field of (24) and (25) for (a) an SS OH regime with $K_{NI} = 0.10$ and (b) an SS ITB regime with $K_{NI} = 0.87$, with $\chi = \chi_{sh}$ ($\alpha = 1.0$), $\mu = 0.01$, $C_\Omega = 0.01$, $C_{BS} = 0.1$, $K_{ext} = 1.9$ and $h(x, y) = 1$. Blue and orange lines are the x- and y-nullclines, respectively, the red and green curves correspond to trajectories with different initial conditions, the black dots indicate the stable fixed points $\{x_{SS}, y_{SS}\}$ and the grey dot an unstable fixed point.

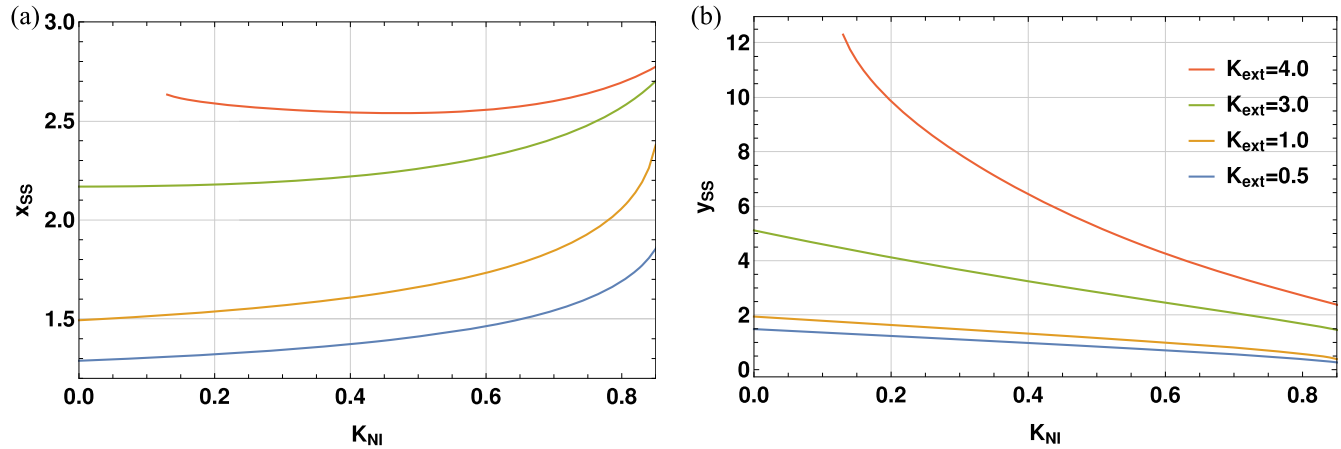

Figure 8. Stable fixed points x_{SS} and y_{SS}, respectively (a) and (b), as functions of K_{NI} for different K_{ext} and with $\chi = \chi_{sh}$ ($\alpha = 1.0$), $C_\Omega = 0.01$, $C_{BS} = 0.1$ and $h(x, y) = 1$.

some point can no longer be arbitrarily small, but it must fulfil the condition $y(0) > y(0)_{\min} > 0$ so that the system is attracted to its stable fixed point. This has to do with the dependency of χ on y: if $y(0)$ is small, then $\chi(0)$ is also small and, with a large $K_{\rm NI}$ that prevents y from increasing too much, the diffusivity keeps a low-enough value that inhibits the losses from compensating the external heating.

3.2.2. ITB oscillations? Regarding current and temperature oscillations, as already mentioned, these are due to the nonlinear coupling between the equations that model their evolution. This coupling comes about via Spitzer's resistivity, heat diffusivity, the BS and externally driven NI currents and their respective power depositions [5, 7, 8, 11, 14, 15]. The first two coupling sources (resistivity and diffusivity) are not sufficient, at least within our model, to trigger oscillations. A scan in $K_{\rm ext}$, $K_{\rm NI}$ and α (and also in μ for reasons that become clearer soon) was made to look for LC's, and the result was null for both diffusivity models considered so far. This indicates that the external NI current density and/or its power deposition should be x and y dependent, in order to introduce a new form of coupling. In the LH case, wave propagation and absorption are usually described having recourse to ray-tracing or full-wave codes [26]. Obviously we are not interested here in this type of approach, so we must do with simple scalings. Since it has been reported that the local LH absorption increases with electron temperature, whereas the global LH efficiency grows with plasma current [11], it is reasonable to assume $S_{\rm ext} \propto jT$. This cross term between T and j for the source is not new, having already been used within the CRONOS transport code [7, 8, 11]. True, it was used to model the LH-driven current density inside the barrier, and not the external heating profile, but since the former typically follows the latter, we adopt the same scaling. Thus, we keep the fraction $K_{\rm NI}$ of externally applied NI current at the foot of the barrier as constant, but write the external heating term due to LH waves as $h(x,\ y) = xy$. Furthermore, note that we have been treating $K_{\rm ext}$ and $K_{\rm NI}$ as independent free parameters so far. In principle, for an LH system, these two quantities should be related although, with the simple arguments used to model the power deposition, it is difficult to tell the scaling of one with the other. Thus, we will keep treating these two as independent and, with this in mind, let us analyse the oscillatory regimes found with the two forms of the diffusivity.

3.2.3. ITB oscillations with χ_{sh}. When the shear diffusivity (16) is used and α is set to 1, supercritical AH bifurcations (i.e. stable LC's) are found for $0 < K_{\rm NI} < 1.0$ and, for each value of $K_{\rm NI}$, for $K_{\rm ext}$ above $K^*_{\rm ext}$, which is the value of $K_{\rm ext}$ at the bifurcation point[8]. Moreover, these oscillations only appear if the time-scale ratio verifies $\mu \approx 1$. In figure 9 we show the phase space of some of these LC's for different values of $K_{\rm ext}$ and $K_{\rm NI} = 0.7$. Observe that, as $K_{\rm ext}$ increases,

[8] For $\alpha = 0.1$, stable LC's were also found, but the oscillations in that case are established around $x \approx 50$, which is way above what is seen in the various experiments.

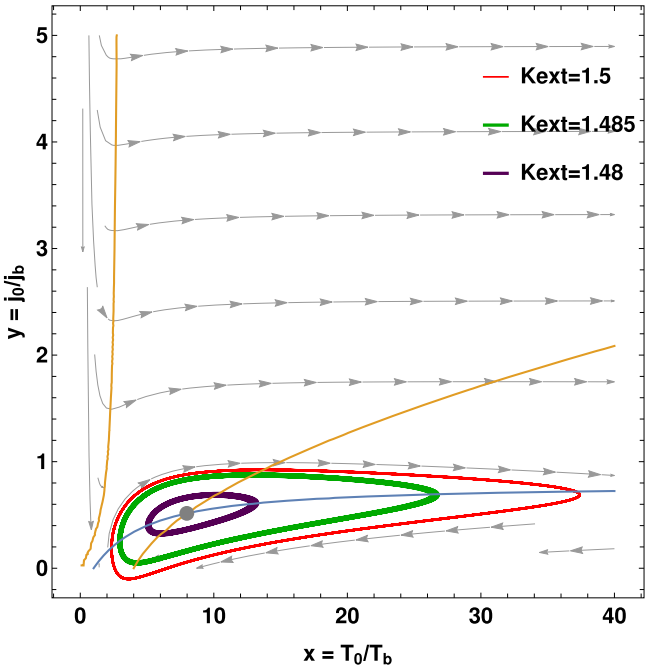

Figure 9. Phase space and vector field of (24) and (25) for different $K_{\rm ext}$, with $\chi = \chi_{\rm sh}$ ($\alpha = 1.0$), $\mu = 1.0$, $C_\Omega = 0.01$, $C_{\rm BS} = 0.1$, $K_{\rm NI} = 0.7$ and $h(x, y) = xy$. Blue and orange lines are the x- and y-nullclines, respectively, and the grey dot indicates the unstable fixed point when $K_{\rm ext} = 1.48$. In this plot, we ignore the initial instants where the trajectories, coming from different initial conditions, approach the respective LC's.

so does the size of the limit cycle, as predicted for AH bifurcations, an increase in size that scales with $\sqrt{K_{\rm ext} - K^*_{\rm ext}}$ [17]. Note it may happen that, for $K_{\rm ext}$ above a certain value, the oscillation in y goes to negative values and this is out of the validity of the model since, for $y < 0$, not only (16) becomes negative (which is non-physical), but we may enter the current-hole domain [27, 28] (which is not covered here). In addition, situations where x becomes less than 1 should be regarded as non-physical too. As $K_{\rm ext}$ increases, $y(0)$ and $x(0)$ cannot be too large, otherwise the system is not attracted to the LC but diverges away instead, which is simply due to the external heating being proportional to xy.

3.2.4. ITB oscillations with χ_{BgB}. Considering the BgB heat diffusivity (23), supercritical AH bifurcations are found when $K_{\rm NI} > 0.5$ and, for each value of $K_{\rm NI}$, when $K_{\rm ext}$ lies above the bifurcation point. However, for this to occur, α must lie roughly in the interval $0.1 \lesssim \alpha \lesssim 0.01$, otherwise no stable, physical LC's are found. When the values of $K_{\rm ext}$ and $K_{\rm NI}$ are not in the LC range, SS ITB regimes are encountered that are much more pronounced than those of the constant external heating case, in the sense that $x_{\rm SS} \gg 1$ and $y_{\rm SS} \ll 1$. An example of this is shown in figure 10, whereas in figure 11(a) we plot a stable LC, whose corresponding oscillations in time are depicted in figure 11(b). Note that the current is in advance of the temperature with a phase shift of 55°, this angle increasing with increasing $K_{\rm ext}$.

No LC's are found when the BgB heat diffusivity is used without the shear correction, nor when the BS term is

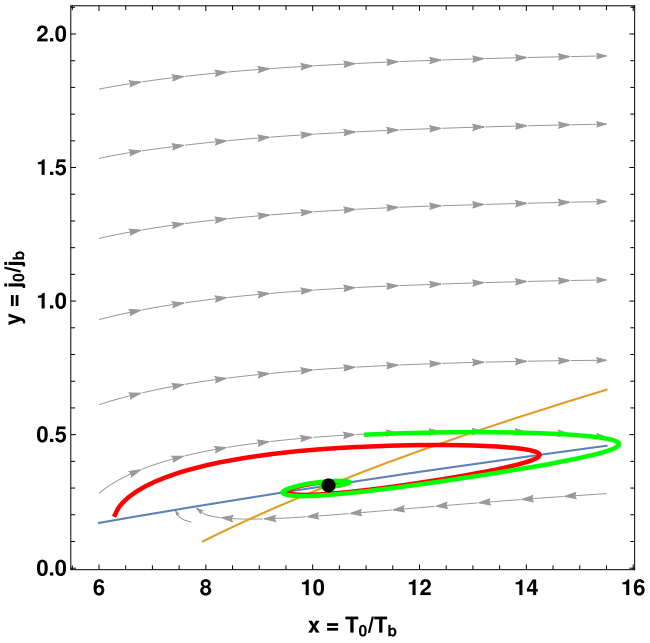

Figure 10. Phase space and vector field of (24) and (25) with $\chi = \chi_{BgB}$ ($\alpha = \gamma = 0.01$), $\mu = 1.0$, $C_\Omega = 0.001$, $C_{BS} = 0.1$, $K_{NI} = 0.4$, $K_{ext} = 0.6$ and $h(x, y) = xy$. Blue and orange lines are the x- and y-nullclines, respectively, red and green curves correspond to trajectories with different initial conditions and the black dot indicates the stable fixed point.

disregarded, and, once more, the oscillations only appear when we set $\mu \approx 1$. From a dynamical system point of view this is understandable: in order to have an oscillatory regime, we need the two quantities competing with each other (just like in a predator-prey system) and this is only possible if both evolve on the same time scale. From a plasma point of view, this means one of three things: the heat transport time τ_x increases to the order of the current diffusion time τ_y, the latter decreases to the order of the former, or a mixing between these two. This last option seems very plausible because, locally close to the ITB, we expect the confinement time to substantially increase and the current diffusion time to be low (due to the small ITB radius), and thus these two times approach each other.

The oscillation frequency in our model is of the order $0.1/\tau_y$, as can be seen in figure 12, where we plot the normalized (i.e. to τ_y^{-1}) frequency f^* as a function of K_{ext}. We also show the frequency curve theoretically predicted by the Hopf theorem, which is given by $\mathrm{Im}(\lambda)/2\pi$, where λ is the eigenvalue of the unstable fixed point at the bifurcation. This formula is exact at the bifurcation point and correct within $\mathcal{O}(K_{ext} - K^*_{ext})$ for K_{ext} close to K^*_{ext} [17]; this is why the predicted value is only in very good agreement with the frequency obtained with the simulation in the beginning, close to K^*_{ext} (which is $K^*_{ext} = 1.30$ in the case of $K_{NI} = 0.6$, as in figure 12). The order of magnitude obtained for f^* means that the period of oscillation is about $10\tau_y$, roughly one order of magnitude above what is seen in the various experiments, in which the oscillation period compares typically with the resistive time [7–9, 11].

4. Discussion of the 1-D model: results from the transport equations

4.1. Implementing the equations

The 0-D model has given us a great insight into the transport equations, providing us with a very simple tool to look at stationary and oscillatory ITB regimes. However, three issues remain to be addressed with the more accurate 1-D equations, namely: the mismatch between the time scales for the two equations, the oscillation frequency and how the amplitude depends on the latter. This is why we now solve the 1-D equations using the same assumptions made for the 0-D model: quadratic profile for the external NI current density between the core and the foot of the barrier, fixed values of temperature and current density at the foot of the barrier and a phenomenological model for the heat diffusivity that takes into account its reduction in RS scenarios.

4.1.1. Numerical scheme. The 1-D equations to be numerically solved are (1) and (3), and the reason why we now prefer to use (3) instead of (2) is that, when using model (14) for the diffusivity, we need the shear s given in (15). The latter is directly given by differentiation of B_θ, whilst if we use j instead we have to perform an integration, which is not so straightforward nor intuitive when working with finite differences as we do. The 1-D equations, to be solved in the interval $\rho \in [0, 1]$, with $\rho \equiv r/r_b$, read

$$\tau_x \partial_t T = \frac{2}{3}\frac{\partial_\rho}{\rho}\left(\frac{\chi}{\chi_0}\rho\partial_\rho T\right) + C_\Omega{}'\frac{j^2}{T^{3/2}} + F_{ext}(T, B_\theta) \quad (27)$$

and

$$\tau_y \partial_t B_\theta = \partial_\rho\left[\left(\frac{T_b}{T}\right)^{3/2}\frac{\partial_\rho(\rho B_\theta)}{\rho}\right] - \mu_0 j_b r_b K_{NI}\partial_\rho\left[\left(\frac{T_b}{T}\right)^{3/2}\rho^2\right], \quad (28)$$

where $C_\Omega{}' = 1.375 r_b^2/n_{20}\chi_0$. The spatial derivatives of the equations are discretized using second-order finite differences and the system is evolved in time according to a semi-implicit numerical scheme, which is to be reported elsewhere and allows us to see an oscillatory regime when we make $F_{ext} \propto jT$ [29]. It is worth mentioning that, had we used one of the standard schemes commonly employed to solve diffusion-like PDE's, such as Crank–Nicolson's, the time evolution would become unstable for the same source term.

4.1.2. Boundary conditions. Since we are interested in comparing results from the 1-D equations with the 0-D dynamical system, boundary conditions for T and j (or B) are taken (as far as possible) the same for both models. Regarding the temperature equation, the exact same boundary conditions have been used, namely, $\partial_\rho T(\rho = 0) = 0$ and $T(\rho = 1) = T_b$. Note that $\nabla T = 0$ on the axis results from requiring that the heat flux $\mathbf{q}$ at the origin be zero. This is so because the cylindrical geometry imposes all fluxes to vanish

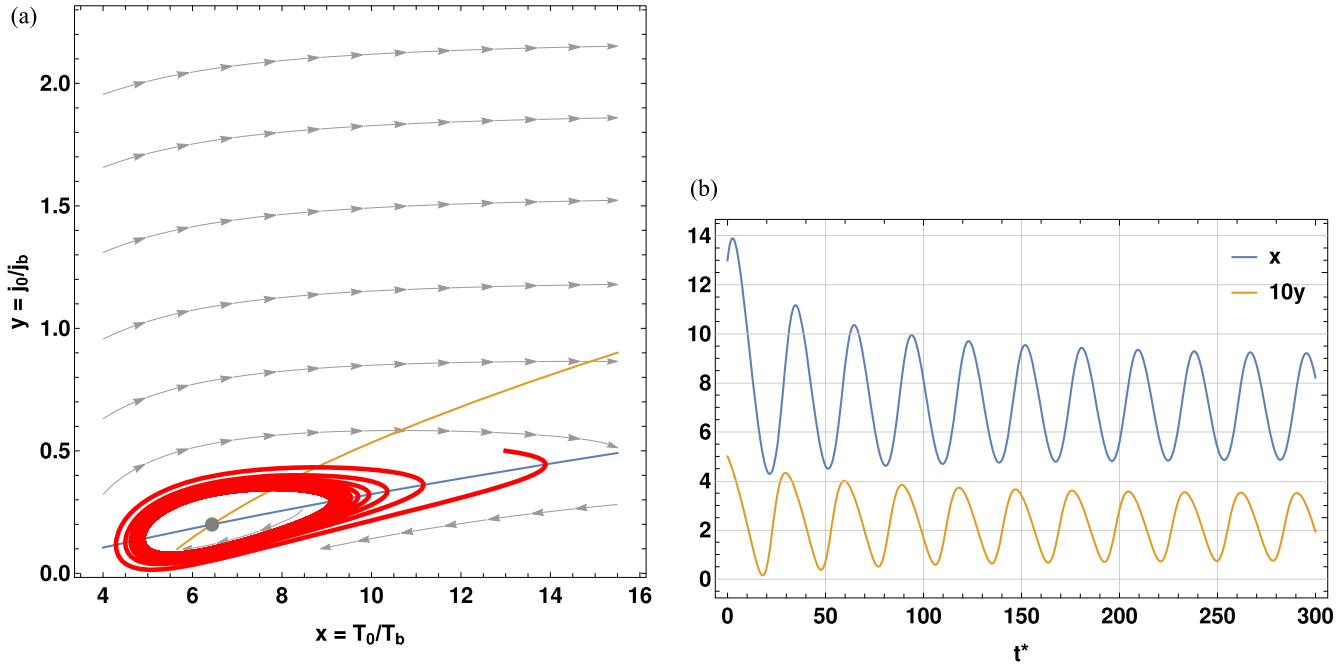

Figure 11. (a) Phase space and vector field of (24) and (25) and (b) temperature and current density oscillations in normalised time $t^* = t/\tau_y$ for stable LC oscillations with $\chi = \chi_{\mathrm{BgB}}$ ($\alpha = \gamma = 0.01$), $\mu = 1.0$, $C_\Omega = 0.001$, $C_{\mathrm{BS}} = 0.1$, $K_{\mathrm{NI}} = 0.60$, $K_{\mathrm{ext}} = 0.55$ and $h(x, y) = xy$. In (a), blue and orange lines are the x- and y-nullclines, respectively, and the grey dot indicates the unstable fixed point.

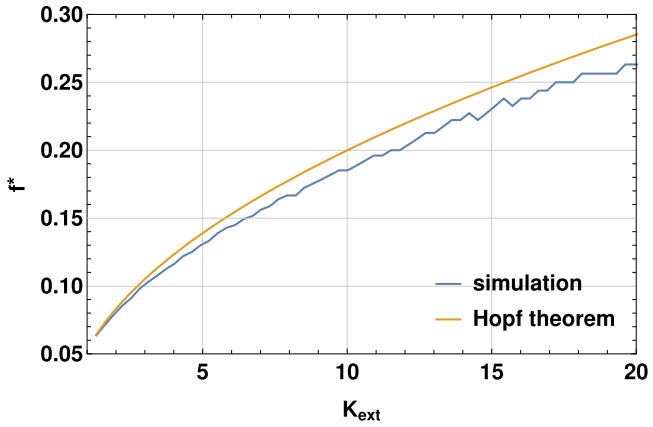

Figure 12. Normalized frequency $f^* = f/\tau_y^{-1}$ of the LC as a function of K_{ext} for $\chi = \chi_{\mathrm{BgB}}$ ($\alpha = \gamma = 0.01$), $\mu = 1.0$, $C_\Omega = 0.001$, $C_{\mathrm{BS}} = 0.1$, $K_{\mathrm{NI}} = 0.6$ and $h(x, y) = xy$. The model frequency is compared with the one given by the Hopf theorem, which is only exact near $K^*_{\mathrm{ext}} = 1.30$ in this case.

at $\rho = 0$; were the flux not exclusively diffusive, ∇T would not be necessarily zero.

As for the j equation, in the case of the 0-D model we have used $\partial_\rho j(\rho = 0) = 0$ and $j(\rho = 1) = j_{\mathrm{b}}$. The former does not follow from the geometry, but it is rather an approximation motivated by the fact that, in SS, equation (3) with Spitzer's resistivity yields

$$\frac{1}{T^{3/2}}(j - j_{\mathrm{NI}}) = C \Rightarrow j = j_{\mathrm{NI}} + CT^{3/2}, \tag{29}$$

where C is an integration constant. It thus follows directly that, in SS,

$$\partial_\rho j(\rho = 0) = \partial_\rho j_{\mathrm{NI}}(\rho = 0) + \frac{3}{2}CT(0)^{1/2}\underbrace{\partial_\rho T(\rho = 0)}_{=0}. \tag{30}$$

This means that, if $\partial_\rho j_{\mathrm{NI}}(\rho = 0) = 0$ (which is the case when using a quadratic profile), we automatically get $\partial_\rho j(\rho = 0) = 0$. Thence, this condition is exact once an SS is achieved, although it may not be true in the transient phase. In the 1-D model, where we use the equation for B_θ instead of the equation for j, the boundary condition on the axis is valid at all instants of time since it follows directly from Ampère's law that

$$\begin{aligned} B_\theta(r = 0) &= \frac{\mu_0}{r}\int_0^r r' j(r')dr'\Big|_{r=0} \\ &= \mu_0 \lim_{r=0} \frac{d}{dr}\int_0^r r' j(r')dr' = \mu_0 \lim_{r=0} rj(r) = 0, \end{aligned} \tag{31}$$

where we have used Cauchy's rule.

Coming now to the condition $j(\rho = 1) = j_{\mathrm{b}}$, which is used both in the 0-D and 1-D models, it may be a little harder to motivate since it is not commonly found in the fusion literature dealing with transport codes [30, 31]. In fact, these codes usually solve the transport equations in the whole plasma volume, using as boundary conditions the total plasma current, or the poloidal flux at the edge. However, in this work we are mainly interested in what happens between the core and the foot of the barrier, which is why we have restricted the equations to that region of the plasma. Experimental data (plus reconstruction by means of integrated

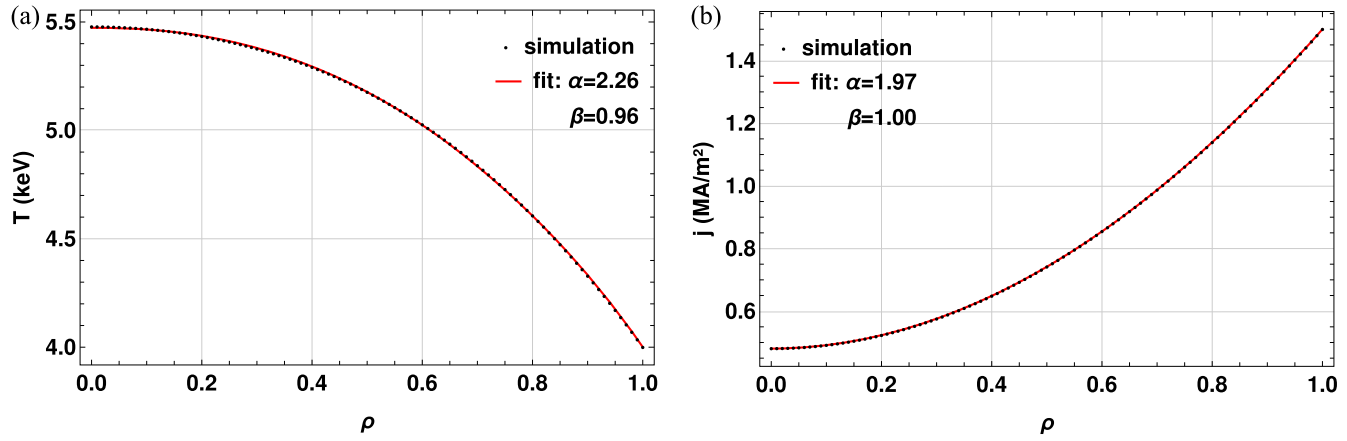

Figure 13. SS profiles of temperature and current density, respectively (a) and (b), for $\chi = \chi_{sh}$ ($\alpha = 1.0$), $K_{NI} = 0.8$ and $K_{ext} = 0.4$. A fit to T of the type $T_{fit}(\rho) = T_b + (T_0 - T_b)(1 - \rho^{\alpha})^{\beta}$ and a similar fit to j are also shown.

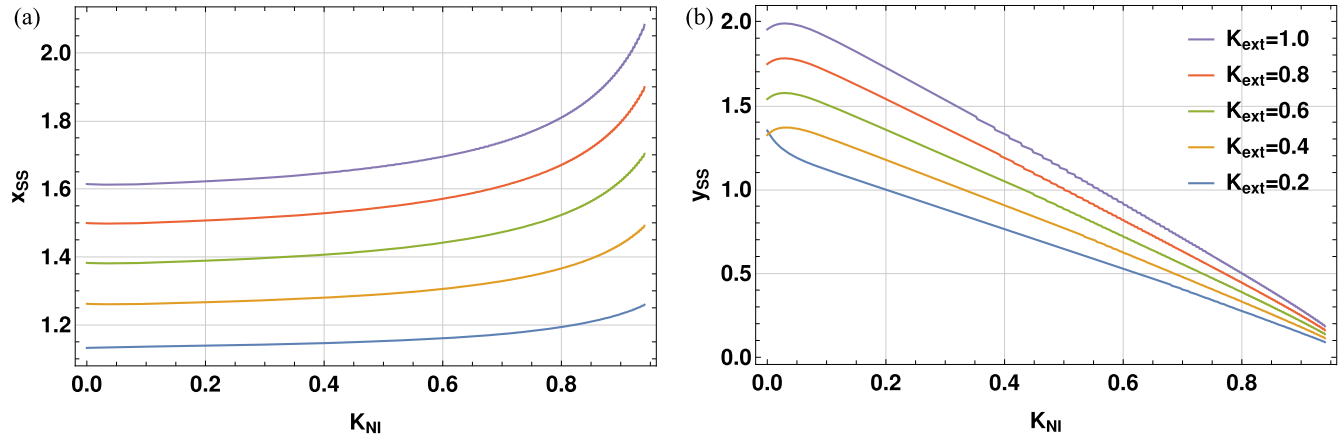

Figure 14. Central SS values $x_{SS} = T_0/T_b$ and $y_{SS} = j_0/j_b$, respectively (a) and (b), as a function of K_{NI} for different K_{ext}, with $\chi = \chi_{sh}$ ($\alpha = 1.0$). Note that the system changes from an OH regime into an ITB regime as K_{NI} increases.

modelling) for the O-regime shows that temperature and current density are approximately constant at the foot of the barrier, even when there are oscillations inside the barrier [8]. This gives us some confidence that the chosen boundary conditions are indeed a quite good approximation.

4.2. Examining SS OH and ITB regimes

Let us start by analysing the SS regimes of the 1-D equations when $\chi = \chi_{sh}$, as given by (14), $F_{ext} = T_b K_{ext}$ is constant and $j_{NI} = j_{ext}(\rho) = K_{NI} j_b \rho^2$ (we do not consider the BS current in the 1-D model). In figures 13(a) and (b) we show, for $K_{NI} = 0.8$ and $K_{ext} = 0.4$, an SS regime obtained by feeding some initial profiles to the numerical scheme and then evolving in time the equations until the profiles no longer change. Note that the SS profiles are essentially quadratic, a feature that is constantly obtained after carrying out this exercise for a broad range of K_{ext} and K_{NI} values. Furthermore, we have also used higher-than-quadratic initial profiles and the system has always evolved towards the same type of quadratic SS profiles, which somehow comforts us in our approach for the 0-D model, where we have assumed quadratic profiles.

We now evaluate SS profiles for different K_{ext} and with K_{NI} in the range $0.0 \leqslant K_{NI} \leqslant 0.95$. After doing so, we can construct the plots in figures 14(a) and (b), where x_{SS} and y_{SS} correspond to the central SS values of T and j normalized to the fixed values at the boundary, very much like in the 0-D model. As expected, we see that larger heating leads to higher core temperatures, and also that, as the fraction of NI current applied at the foot of the barrier is increased, so does the temperature. At the same time, we see that the current density changes from an OH profile to a more reversed profile as K_{NI} increases and, moreover, that the central current density increases with K_{ext}. These observations are all in accordance with the results of the 0-D model, as can be checked by comparing figures 14(a) and (b), on the one hand, with figures 8(a) and (b), on the other. We stress that this behaviour of changing from an OH to an ITB regime is induced by the type of heat diffusivity used. More precisely, if χ had not a shear dependency, the temperature equation would be decoupled from the magnetic field equation (aside from the OH heating term, which has little influence since $K_{ext} \gg C_{\Omega}$), and thus x_{SS} would not be sensitive to K_{NI}.

4.3. Analysing oscillatory ITB regimes

When we make $F_{ext} = K_{ext} jT/j_b T_b \propto jT$, we are able to find oscillations when $0.01 \lesssim \mu \lesssim 1$, which is a much lesser

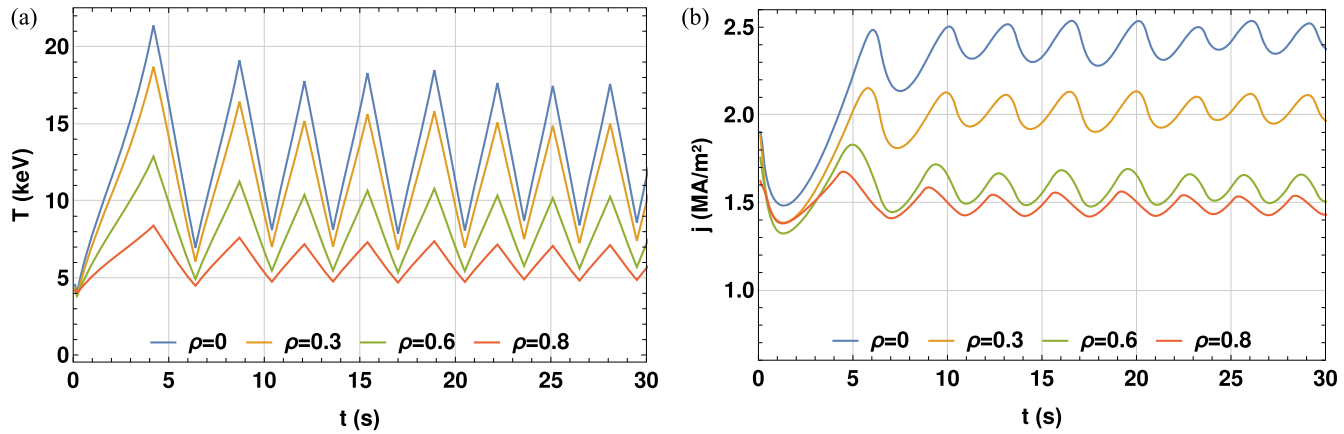

Figure 15. Temperature and current density oscillations, respectively (a) and (b), at different ρ positions with $\chi = \chi_{sh}$ ($\alpha = 1.0$), $\mu = 0.3$, $K_{NI} = 0.7$ and $K_{ext} = 7.5$.

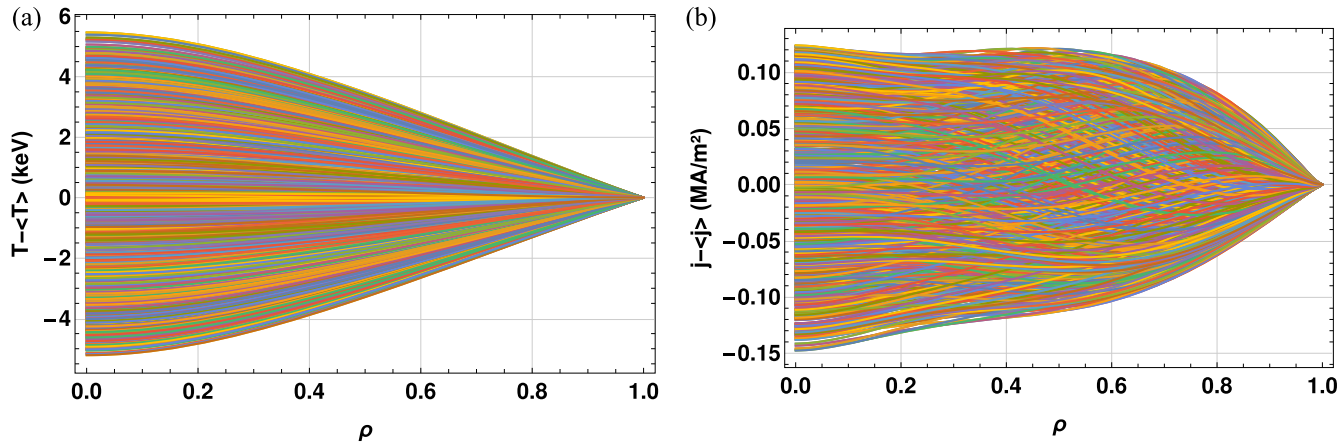

Figure 16. Temperature and current density envelopes during oscillations, respectively (a) and (b), constructed by superposing the profiles $T - \langle T \rangle$ and $j - \langle j \rangle$ for several oscillating cycles, with $\langle T \rangle$ and $\langle j \rangle$ average values and for the same simulation parameters of figures 15(a) and (b).

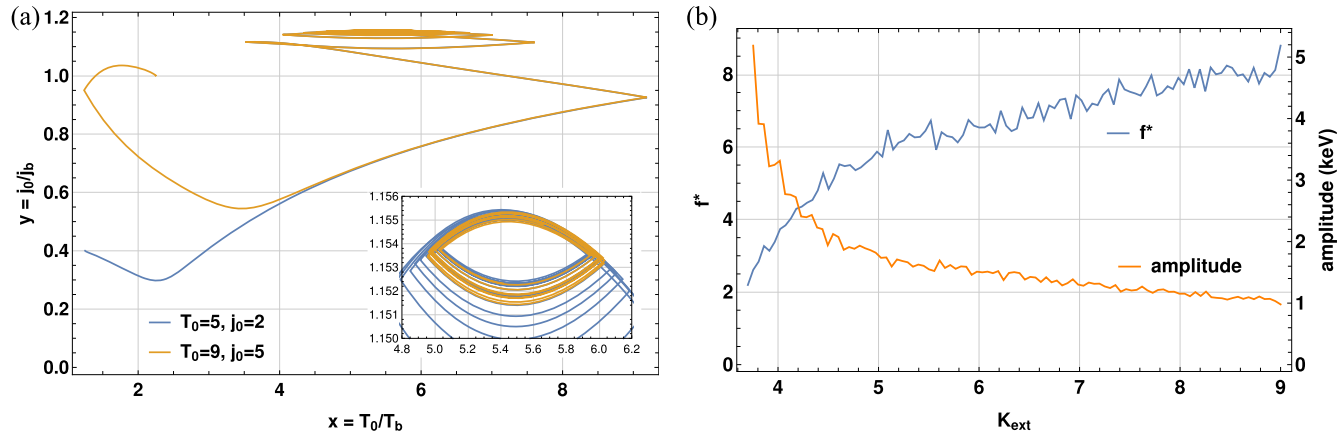

Figure 17. (a) Phase space of $x = T_0/T_b$ and $y = j_0/j_b$ for $K_{ext} = 4.5$ and two different initial conditions and (b) normalized frequency $f^* = f/\tau_y^{-1}$ of the LC and amplitude of the temperature oscillations as functions of K_{ext}, with $\chi = \chi_{sh}$ ($\alpha = 1.0$), $\mu = 0.3$ and $K_{NI} = 0.7$. In (a), note that the same LC is achieved for both initial conditions.

constraint than the 0-D model condition $\mu \approx 1$. Furthermore, contrary to the 0-D model, all the oscillatory regimes within the 1-D equations were obtained without the BS term, thus making jT the main term inducing a nonlinear coupling between T and B, which ultimately leads to oscillations. The appearance of oscillations is very similar to the bifurcation-like behaviour we have seen in the dynamical system, 0-D model: for a fixed value of K_{NI}, an oscillatory regime appears

after a certain K^*_{ext} threshold. In figures 15(a) and (b) it is depicted an example of the oscillations at different ρ positions, with the oscillations in j looking more sinusoidal than those in T, the latter very much resembling the O-regime in Tore Supra [7, 8, 11]. The corresponding envelopes, once a stable oscillatory regime has been established, are shown in figures 16(a) and (b), where it is possible to see the symmetry of the oscillations about their average values. Moreover, we can see that the oscillation amplitude is larger in T than in j.

It is also interesting to observe that different initial profiles lead to the same LC, in the same manner as we have seen above that, after the transient regime, different initial profiles lead to the same SS. This can be verified in figure 17(a), where we have used as initial profiles $T(\rho) = T_0 - (T_0 - T_b)\rho^2$ (and a similar one for j) with $\{T_0/\text{keV},\ j_0/\text{MA m}^{-2}\} = \{5.0,\ 2.0\}$ and $\{T_0/\text{keV},\ j_0/\text{MA m}^{-2}\} = \{9.0,\ 5.0\}$, and have plotted the corresponding trajectories in phase space. The oscillation frequency was also studied in the context of the 1-D model and we show in figure 17(b) the normalized frequency f^* as a function of K_{ext}, for $K_{NI} = 0.7$, the bifurcation point occuring at $K^*_{ext} = 3.7$ for $T_0 = 20\,\text{keV}$[9]. It must be noted that f^* increases with K_{ext} just like in the 0-D model, where the Hopf theorem predicted such increasing. The main difference with the 0-D model lies in the frequency itself, since now we have a frequency of the order of τ_y^{-1} or, in other words, an oscillation period of the order of τ_y, instead of $10\tau_y$ as in the 0-D case. The 1-D results thus agree more correctly with the experiments, since in the O-regime the oscillation is commensurate with the resistive time scale [7, 8, 11]. Regarding the oscillation amplitude itself, more precisely, how it varies with K_{ext}, we see that it is always smaller than 10 keV. At Tore Supra, it was reported that the amplitude of the temperature oscillation ranged from 0.1 to 1.0 keV [7], meaning that our 1-D model can reproduce the correct amplitude in a given interval of K_{ext}. We can still see from figure 17(b) that the T oscillation amplitude becomes smaller as K_{ext} increases, which is markedly in contrast with what was seen in the 0-D model, where a growth with K_{ext} was found (as expected from AH bifurcation theory). In any case, what we see in figure 17(b) is exactly what is observed with the O-regime in Tore Supra: decreasing of the oscillation amplitude with increasing frequency [7].

5. Summary and conclusions

In this work, and with the purpose of studying ITB oscillations as those characteristic of the O-regime in Tore Supra [7, 8, 11], a 0-D model in the form of a dynamical system was systematically derived from the 1-D diffusion equations governing electron temperature and current density in fusion plasmas. The said model is not only capable of capturing the ITB oscillatory behaviour, but it also provides the expected SS OH and ITB regimes. Note that the approach followed here is substantially different from a previous attempt to model these ITB oscillations using an *ad-hoc* system of predator-prey equations [8] in that, to arrive at the 0-D dynamical system obtained in this paper, we followed a methodical reduction process starting from the appropriate 1-D transport equations.

Two forms for the heat diffusivity were used, one phenomenological and the other related with the BgB diffusivity (corrected for RS configurations), which were further adapted to our 0-D model. When the external heating and CD terms are set to constants, it is possible to identify a continuous transition from an SS OH to an SS ITB regime as the fraction of externally applied NI current at the foot of the barrier is increased. By recognising that many LC oscillatory regimes in dynamical systems occur whenever an AH bifurcation appears, a scan was made in parameter space to find this bifurcation and then check whether the LC was stable/unstable so that we could give it a physical meaning. When the external terms are constant, no LC's were found; however, stable LC's were encountered, with both forms for the diffusivity, when the external heat source was made proportional to both temperature and current in order to mimic the power deposition of an LH system. Moreover, with this form for the external heating, SS ITB regimes exist when the free parameters of the model are not in the LC range.

A feature of the oscillations found with the 0-D model is that they only appear when the time scales of the two equations are commensurate, meaning that the characteristic heat transport and current diffusion times must be of the same order (i.e. their ratio must be roughly 1). In fact, this should be experimentally expected also because, at the ITB (where confinement happens to be significantly higher), the time scales for heat transport and current diffusion (within a small ITB radius) tend to become similar. It was further shown that a necessary condition to see LC oscillations is to have a current dependency in the heat diffusivity (which we have assumed to be of the type that reduces the latter in RS configurations). This manifestly indicates that the true, actual heat transport coefficient must be shear (or current) dependent, something that has been intuited [15, 24], but whose clear demonstration is still lacking. We can even envisage, in the future, to infer the type of interplay, or coupling, between the transport and current equations in AT scenarios by analysing these ITB oscillations. For instance, this can be done by varying the functional dependency on current of the heat diffusivity, then comparing the obtained oscillations with what is experimentally observed and subsequently, if necessary, iterating the procedure.

There are two additional features of the 0-D model oscillations that do not match the experimental results, namely: the oscillation period, which is one order of magnitude above the experiment, and the LC amplitude, which increases with frequency, the opposite of what was reported for the O-regime. For that reason, we decided to solve the more exact 1-D transport equations with the same type of assumptions that led us to the 0-D dynamical system. By doing this, we were able to obtain oscillations with a period whose order of magnitude matches that of the resistive time scale and whose amplitude becomes smaller as the frequency grows, precisely the trends seen in the experiment [7, 8, 11].

[9] We indicate T_0 because we have seen that the bifurcation point varies (but not very much) with it.

We have seen in both models that, once beyond the bifurcation point, the oscillations are persistent and cannot be made to disappear by augmenting the external heating, which is in accordance with previous results showing that, in order for the oscillatory behaviour to vanish, the $E \times B$ shear must play a role in the χ model [5], something we have not accounted for herein. It has been observed as well that precise shapes of the ECCD deposition profiles are necessary to overcome the oscillations in the O-regime [8], still a further element not considered in our models. There is thus room for improving our 0-D analysis, through the incorporation of these mechanisms in the χ models utilized, in order to conclude whether, after the bifurcation point that leads to LC oscillations, another bifurcation appears that kills them or not. One last comment: the oscillations found within the 1-D model were obtained with equations that do not include in them the contribution of the BS current, differently from the 0-D model, where keeping the BS term is a necessary condition to get LC oscillations. Hence, a work to be done, and which would be of relevance for the SS operation of future fusion reactors, is to analyse ITB oscillations, from a dynamical system point of view, in the BS-dominated regime seen in DIII-D [10] and studied for AT scenarios in JET [5, 16].

Acknowledgments

Fruitful discussions with Rui Vilela Mendes are gratefully acknowledged.

This work received financial support from Fundação para a Ciência e a Tecnologia (FCT, Lisboa) through projects No. UID/FIS/50010/2013 and No. UID/FIS/50010/2019. Part of it was conducted under the European Fusion Development Agreement (EFDA) and the Contracts of Association between Euratom and IST and between Euratom and the Commissariat à l'Énergie Atomique (CEA), and received financial support through the contract of Laboratório Associado with FCT. BFAS was supported by FCT under grant No. SFRH/BD/42535/2007. The views and opinions expressed herein do not necessarily reflect those of the European Commission, of FCT, of IST or of their services.

ORCID iDs

A J Coelho https://orcid.org/0000-0002-8889-7259
João P S Bizarro https://orcid.org/0000-0002-0698-6259

References

[1] Gormezano C *et al* 2007 *Nucl. Fusion* **47** S285
[2] Connor J W *et al* 2004 *Nucl. Fusion* **44** R1
[3] Joffrin E 2007 *Plasma Phys. Control. Fusion* **49** B629
[4] Litaudon X *et al* 2007 *Nucl. Fusion* **47** 1285
[5] Bizarro J P S *et al* 2007 *Nucl. Fusion* **47** L41
[6] Freidberg J P 2007 *Plasma Physics Fusion Energy* (Cambridge: Cambridge University Press)
[7] Giruzzi G *et al* 2003 *Phys. Rev. Lett.* **91** 1
[8] Turco F *et al* 2009 *Phys. Plasmas* **16** 062301
[9] Coda S *et al* 2007 *Nucl. Fusion* **47** 714
[10] Politzer P A *et al* 2005 *Nucl. Fusion* **45** 417
[11] Imbeaux F *et al* 2004 *Proc. 10th IAEA Fusion Energy Conference (Vilamoura, Portugal)*
[12] Maget P *et al* 2006 *Nucl. Fusion* **46** 797
[13] Turri G *et al* 2008 *Plasma Phys. Control. Fusion* **50** 065010
[14] Fukuyama A *et al* 1995 *Nucl. Fusion* **35** 1669
[15] Voitsekhovitch I and Moreau D 2001 *Nucl. Fusion* **41** 845
[16] Bizarro J P S *et al* 2008 *IEEE Trans. Plasma Sci.* **36** 1090
[17] Strogatz S H 2000 *Nonlinear Dynamics and Chaos: With Applications to Physics, Biology, Chemistry and Engineering* (Colorado: Westview Press)
[18] Staebler G M and Groebner R J 2015 *Plasma Phys. Control. Fusion* **57** 014025
[19] Itoh S I *et al* 1991 *Phys. Rev. Lett.* **67** 2485
[20] Wu X *et al* 2015 *Nucl. Fusion* **55** 053029
[21] Weymiens W *et al* 2012 *Phys. Plasmas* **19** 072309
[22] Wesson J 2001 *Tokamaks* 3rd edn (Oxford: Oxford Science Publications)
[23] Voitsekhovitch I *et al* 1997 *Nucl. Fusion* **37** 1715
[24] Parail V V *et al* 1999 *Nucl. Fusion* **39** 429
[25] Bizarro J P S *et al* 2016 *Plasma Phys. Control. Fusion* **58** 105010
[26] Bonoli P T 2014 *Phys. Plasmas* **21** 061508
[27] Rodrigues P and Bizarro J P S 2005 *Phys. Rev. Lett* **95** 015001
[28] Rodrigues P and Bizarro J P S 2007 *Phys. Rev. Lett.* **99** 125001
[29] Bizarro J P S, Venâncio L and Mendes R V 2019 arXiv:1905.04520
[30] Artaud J F *et al* 2010 *Nucl. Fusion* **50** 043001
[31] Pereverzev G V and Yushmanov P N 2002 *IPP-Report* IPP 5/98 Max-Planck-Institut für Plasmaphysik